Comparative Electron and Photon Excitation of Localized Surface Plasmon Resonance in Lithographic Gold Arrays for Enhanced Raman Scattering

SCHOLARONE™
Manuscripts

ARTICLE

Comparative Electron and Photon Excitation of Localized Surface Plasmon Resonance in Lithographic Gold Arrays for Enhanced Raman Scattering

Yitian Zeng,*[a] Steven J. Madsen, [a] Andrew B. Yankovich, *[b] Eva Olsson [b] and Robert Sinclair [a]

The ability to tune the localized surface plasmon resonance (LSPR) of nanostructures is desirable for surface enhanced Raman spectroscopy (SERS), plasmon-assisted chemistry and other nanophotonic applications. Although historically the LSPR is mainly studied by optical techniques, with the recent advancement in electron monochromators and correctors, it has attracted considerable attention in transmission electron microscopy (TEM). Here, we use electron energy loss spectroscopy (EELS) in a scanning TEM to study individual gold nanodiscs and bowties in lithographic arrays with variable LSPRs by adjusting the size, interspacing, shape and dielectric environment during the nanofabrication process. We observe the strongest Raman signal enhancement when the LSPR frequency is close to the incident laser frequency in Raman spectroscopy. A simplified harmonic oscillator model is used to estimate SERS enhancement factor (EF) from EELS, bridging the connection between electron and photon excitation of plasmonic arrays. This work demonstrates that STEM-EELS shows promise for revealing the contributions of specific LSPR modes to SERS EF. Our results provide guidelines to fine-tune nanoparticle parameters to deliver the maximum signal enhancement in biosensing applications, such as early cancer detection.

1 Introduction

The Raman signal from an organic molecule can be significantly enhanced by its contact with a noble metal surface[1–3]. This phenomenon, now known as surface enhanced Raman spectroscopy (SERS), is employed in biological and chemical sensing applications owing to its high sensitivity and fingerprinting accuracy. Applications range from single molecule sensing[2,4], rapid bacteria identification[5], artwork authenticity evaluation[6] to the detection of circulating tumor cells/DNA[7,8] and early stage tumors[9–11]. The latter has clear importance in cancer diagnostics and therapy[12–14].

The SERS enhancement, which can be many orders of magnitude, is generally recognized as mostly arising from the local electric field enhancement associated with surface plasmons in noble metals[3,15], which essentially are the collective oscillation modes of the free electron gas at the metal surface. Noble metal nanoparticles are particularly useful as their localized surface plasmon resonance (LSPR) energies are functions of nanoparticle parameters, such as shape, size and mutual proximity[16–20]. It is also expected that greater enhancement (and so higher signal) would be achieved when the induced plasmons are in resonance with the illuminating photon energies[21,22].

While the LSPR of metallic nanoparticle clusters can be studied by far-field extinction microscopy[23], far-field dark-field optical microscopy[19,24] and near-field optical extinction microscopy[25] techniques, their individual energies and local spatial distributions have been most effectively demonstrated by electron energy loss (EEL) mapping by scanning transmission electron microscopy (STEM). Nelayah et al.[26] first showed the plasmon distributions in 5.5 nm silver nanoprisms, which was expanded by Koh et al.[27] to gold triangular combinations as fabricated by electron beam lithography and to other nanoparticle shapes and sizes[28–30]. In the present work, we have used lithographic methods to systematically vary the shape, interspacing and size of nanoparticles, while studying their effect on LSPR distributions using STEM-EELS. We then compare the LSPR with the Raman signal enhancement from the exact same areas and demonstrate experimentally that the greatest Raman signal enhancement is obtained when the LSPR energy matches that of the exciting laser or Raman emissions. The quantitative experimental results on individual nanoparticles obtained from EELS are consistent with previous reported values on ensemble samples from optical measurements and supported by the boundary element method (BEM) simulations. Accordingly, we show a method to roughly estimate Raman signal enhancement factor (EF) using LSPR measured in EELS based on a harmonic oscillator model, which can be practically used for pre-screening plasmonic nanoparticles directly in TEM. Our

a. Department of Materials Science and Engineering, Stanford University, Stanford, California 94305, United States.
b. Department of Physics, Chalmers University of Technology, Gothenburg 41296, Sweden.
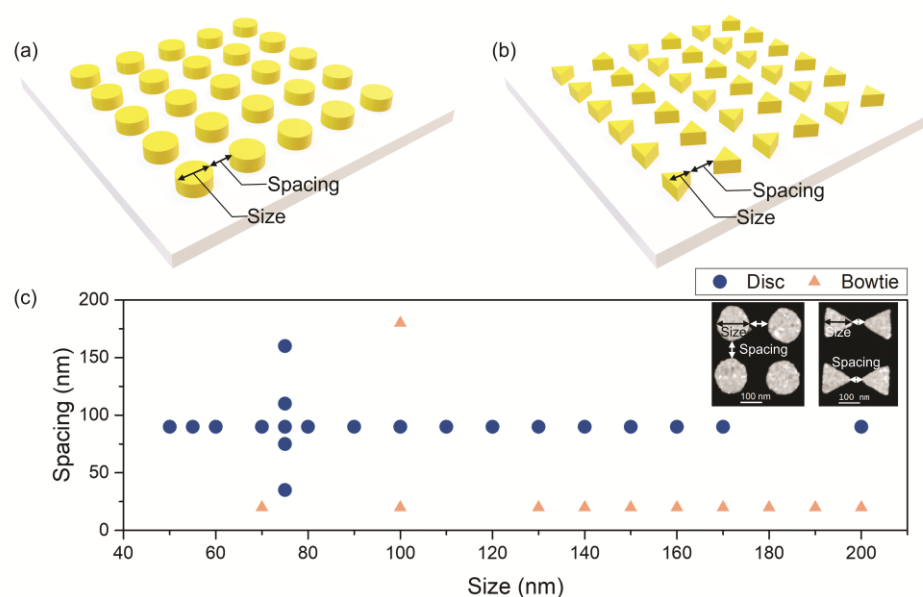
Fig. 1 An overview of geometric parameters of gold nanodisc and bowtie arrays. **(a)** A schematic array of 30 nm thick Au nanodiscs on a 30 nm thick membrane substrate with the size and the spacing defined as the disc diameter and the edge-to-edge distance. **(b)** A schematic bowtie array with the triangle height as the bowtie size and the distance between two pointing vertices as the bowtie spacing. **(c)** Au nanostructures investigated in this work are: nanodisc arrays with diameter from 50 nm to 200 nm and interspacing from 35 nm to 160 nm; bowtie arrays with size from 70 nm to 200 nm and spacing from 20 nm to 180 nm. Insets are part of annular dark field STEM images of the nanodisc and bowtie arrays, with the gold structures being bright in these images. Additional images can be found in **ESI Figs. S1, & S2**.

53 observation when applying this method to bowties also
54 suggests that monochromated STEM-EELS shows promise
55 for revealing the contributions of specific LSPR modes to
56 SERS EF. By comparatively studying both electron and
57 photon excitation of surface plasmons, we propose a
58 procedure to engineer nanoparticles to precise shapes and
59 sizes to yield the highest Raman enhancement, which
60 would then be optimized for practical applications, such as
61 high sensitivity biomarker detection. This combination is
62 unique in our work. Additionally, the conclusions would also
63 benefit other fields utilizing LSPR enhancement, e.g. in solar
64 cells[31], plasmonic nanoparticles with optimized parameters
65 would increase the absorption cross-section and overall
66 efficiency when the LSPR is fully excited by the incident
67 light.

Experimental

69   This work explores gold nanodiscs and bowties with
70 varying size and spacing, fabricated in 2 μm × 2 μm arrays
71 using electron beam lithography for fast prototyping. The
72 procedures have been described in a previous publication[32].
73 The nanodisc size (diameter) and spacing (edge to edge
74 distance) ranged from 50-200 nm and from 35-160 nm,
75 respectively (**Figs. 1a, & c**). The bowtie size (triangle height)
76 and spacing (tip-to-tip distance) ranged from 70-200 nm
77 and from 20-180 nm, respectively (**Figs. 1b, & c**). Both
78 nanodiscs and bowties are 30 nm in thickness. Arrays were
79 fabricated on 35 nm thick SiN_x and SiO_x membranes to
80 enable examination with STEM. Additional details are given
81 in the Methods section. Nanoparticles with desired
82 properties can also be fabricated using scalable techniques,

83 such as optical based fabrication techniques[33] and wet
84 chemical synthesis.

85   During STEM-EELS measurements, a 300 kV electron
86 probe (approx. 0.5 nm diameter) was rastered across a
87 subset of the array (see Methods section for STEM
88 conditions) and EEL spectra were recorded simultaneously
89 at each pixel. Annular dark field (ADF) images of the
90 structures show contrast between different grain
91 orientations (**Fig. 1c insets**), indicating the structures are
92 polycrystalline. After EELS measurements, each array was
93 then tested with two different Raman dye molecules,
94 Rhodamine 6G (R6G) and 4-Mercaptopyridine (4-MP), in a
95 Raman confocal microscope with 532 nm, 638 nm and 785
96 nm wavelength lasers to collect Raman spectra from each
97 array.

Results and discussion

Nanodisc surface plasmons in EELS

100   First, we explore how plasmon excitation varies within a
101 single array (90 nm discs on SiN_x) as a function of electron
102 probe position. Experimental spectra, represented by solid
103 lines, were collected from the nanodisc perimeter (**Fig. 2a**),
104 in the midpoint between four discs (**Fig. 2b**) and at the disc
105 center (**Fig. 2c**).The zero loss peak (ZLP) is used to normalize
106 each spectrum to the same maximum intensity and
107 subsequently subtracted. Simulated EEL spectra, based on
108 the boundary elementary method[34], are plotted as dotted
109 lines in **Figs. 2a, b & c** and show good agreement with the
110 experimental data. These simulations utilized the
111 experimental electron beam energy and nanoparticle size,
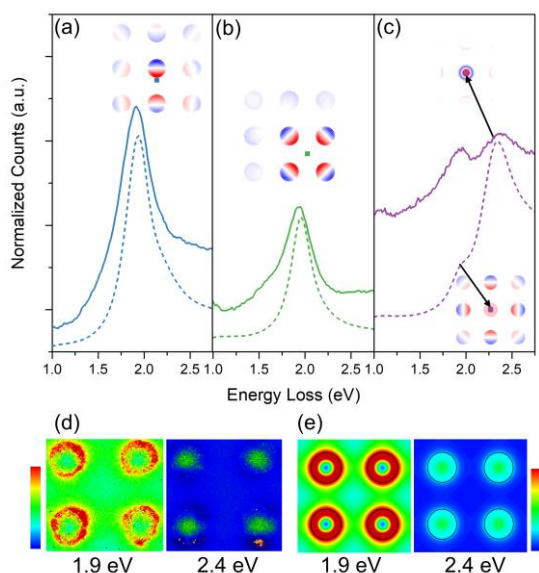
Fig. 2 Localized surface plasmon peaks and the corresponding distribution of 90 nm discs on SiN$_x$ in EELS mapping. EEL spectra (solid lines) and simulated spectra (dotted lines) are integrated from the disc perimeter **(a)**, the midpoint between discs **(b)** and the disc center **(c)**. Simulated charge density distributions are shown in the insets with points of excitation (e-beam locations) labelled correspondingly as blue, green and purple squares. Peaks at 1.9 eV all exhibit dipolar behavior, while the breathing mode (2.4 eV) is only present at the disc center. **(d)** Normalized EELS intensity distributions and **(e)** simulated maps at energy loss of 1.9 eV shows that the dipolar mode is omnipresent across the whole surveyed area but is strongest around the nanodisc perimeters. Maps at energy loss of 2.4 eV reveal that the breathing mode is restricted within the nanodisc center (strong intensities on bottom right of (d) 2.4 eV map is a result of a sharp spike at the edge possibly due to fabrication imperfection). Energy window of EELS maps is 0.01 eV.

112 and were calculated using models composed of nanodisc
113 arrays on a SiN$_x$ or SiO$_X$ substrate that were derived from
114 the real nanostructure geometries (more details in
115 Methods). Because of computational limitations, the
116 models were limited to nine disc arrays (one central disc
117 surrounded by its eight nearest neighbors), which was
118 sufficiently large to capture the experimental behavior. The
119 simulations were also used to predict the corresponding
120 surface charge density distributions at the LSPR peak
121 positions, as shown in the insets in **Figs. 2a, b & c**. A dipolar
122 surface plasmon mode at an energy loss of 1.9 eV, with
123 positive (red) and negative (blue) surface charges
124 distributed on the opposite sides of the disc, is present in all
125 three spectra. A breathing LSPR mode is present at 2.4 eV,
126 as indicated by the radial shape of charge density
127 distribution[35], and is only observed in **Fig. 2c** when the
128 electron beam is positioned at the disc center. However, a
129 plane wave illumination such as light cannot excite the
130 breathing mode because the symmetry of the charge
131 distribution results in a vanishing net dipole moment[32,35].
132 Therefore, this study will primarily focus on the dipolar
133 LSPR.
134   Once the energies of plasmon resonances have been
135 determined, we can plot the plasmon excitation intensity as
136 a function of position. Distributions at the dipolar mode
137 peak of 1.9 eV and the breathing mode peak of 2.4 eV are
138 shown in **Fig. 2d** with each pixel normalized to the ZLP

139 maximum and drawn to the same color scale.
140 Corresponding simulated EELS maps (**Fig. 2e**) show a similar
141 distribution and confirm that the dipolar plasmon mode is
142 omnipresent across the whole array with the most intense
143 peaks residing around the nanodisc perimeters, while the
144 breathing mode is only observed within the metallic
145 nanodiscs.

Effect of nanodisc parameters on LSPR

147   Several nanoparticle parameters, such as size, shape
148 and dielectric environment, have been studied theoretically
149 and experimentally that could affect LSPR[15,20,36]. However,
150 a quantitative and systematic work studying the effect of
151 nanoparticle parameters on LSPR using EELS, compared
152 with SERS enhancement and supported by theory has not
153 been reported before to our knowledge. Experimental EEL
154 spectra from different diameter nanodiscs on SiN$_x$ and SiO$_x$
155 membranes are summed within a 4 nm distance around the
156 nanodisc perimeters in **Figs. 3a, & b**. The measured dipolar
157 surface plasmon peak energies are plotted as a function of
158 nanodisc size from 30 nm to 220 nm in **Fig. 3c**. The
159 interspacing of the mentioned disc arrays is kept at 90 nm.
160 The LSPR energy blue shifts (as expected theoretically[37]) as
161 the nanodisc size decreases, in a linear manner in this size
162 range and can be roughly estimated by $(2.3 - 0.0037d)$ eV
163 for arrays on SiN$_x$ and $(2.6 - 0.0045d)$ eV for arrays on
164 SiO$_x$, where d is the disc diameter from 50 nm to 200 nm.
165 Therefore, nanoparticle size is an important parameter in
166 fine-tuning the localized surface plasmon response of the
167 nanostructure, as is the local dielectric environment. This
168 phenomenon has also been reported in various optical[15,18]
169 and simulation[38] studies. Corresponding EELS simulations,
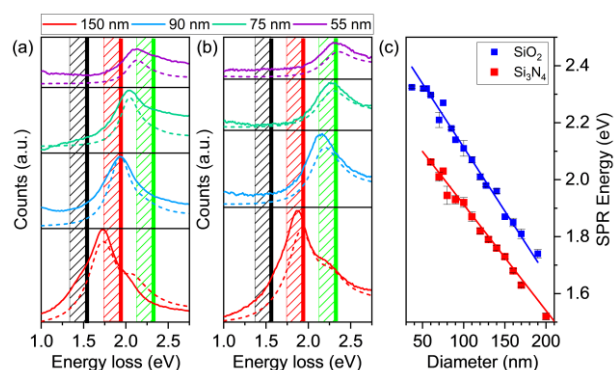
Fig. 3 Nanodisc size and dielectric constant of surrounding medium strongly affect LSPR energy. Integrated EEL spectra around the four discs perimeter showing surface plasmon peaks of various nanodisc size on **(a)** SiN$_x$ (dielectric constant ~4.2) and **(b)** SiO$_x$ (dielectric constant ~2.1) membrane, respectively. There is a clear blue shift (increasing peak energy) with decreasing disc diameter. Dotted lines are simulated EEL spectra of the corresponding nanodisc size in the same color scheme. The bold vertical dark line corresponds to a 785 nm (1.58 eV) laser excitation wavelength, the red line corresponds to a 638 nm (1.94 eV) laser excitation wavelength and the green line corresponds to a 532 nm (2.33 eV) laser excitation wavelength. The shaded area corresponds to the Raman spectra collection range from 550 cm^{-1}~1800 cm^{-1} (0.068 eV ~ 0.22 eV). **(c)** Dipolar peak energies vary approximately linearly with nanodisc size from 30 nm to 220 nm measured in monochromated STEM-EELS. Error bars indicate the range of SPR energies in measured locations.
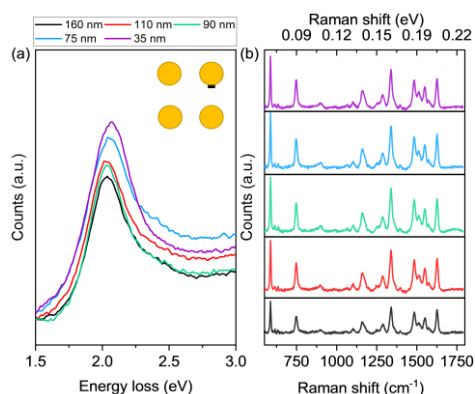
Fig. 4 Nanodisc spacing has a minor effect on LSPR energy and overall Raman signal enhancement. **(a)** Integrated EEL spectra around the nanodisc circumference in arrays at a constant diameter of 75 nm and various edge to edge separation from 35 nm to 160 nm on SiN$_x$ membrane. Only a slight blue-shift (< 0.2 eV) of the dipolar resonance energy when the separation is decreased indicates that interspacing has only a minor effect. **(b)** The corresponding Raman spectra of R6G from the same nanodisc arrays as in (a) measured with a 532 nm laser showing Raman signal enhancement is not strongly affected by the interspacing. The relatively lower Raman signal of 160 nm spaced nanodiscs may arise from a lower fill factor of nanodiscs in the array. The legend is the same as in (a).

170 represented by dotted lines in **Fig. 3a, b,** match the
171 experimental results well.
172   For the same size nanodiscs, we observe that the LSPR
173 energy is strongly dependent on local dielectric
174 environment. In the visible wavelength regime, the
175 dielectric constant for Si$_3$N$_4$ is ~4.2[39] and for SiO$_2$ is ~2.1[40]. A
176 red shift of LSPR energy is shown in **Fig. 3c** when the
177 substrate dielectric constant increases because the
178 polarizability of the system, which is maximum at the
179 resonance frequency, is inversely related to both the
180 dielectric constants of nanoparticles and their surrounding
181 media[15]. A simplified model based on a quasi-static
182 approximation provides reasonable theoretical explanation
183 and can be found in **ESI Fig. S3**. This behavior is important
184 for biological applications as oftentimes plasmonic
185 nanoparticles are coated with functional and/or protective
186 layers (such as silica), which may have different dielectric
187 constants, affecting the resonance energy.
188   Interspacing is of interest due to a possible coupling
189 effect between localized surface plasmons in near field. EEL
190 spectra (**Fig. 4a**) around nanodisc edges in arrays at a
191 constant size of 75 nm and various interspacing from 35 nm
192 to 160 nm share similar shape and intensity. However, the
193 peak position is observed to slightly blue shift (< 0.2 eV) for
194 smaller interspacing due to the generation of bonding and
195 antibonding modes from LSPR hybridization and stronger
196 electrostatic repulsion of like charges[27]. Significant
197 resonance shifts (> 1 eV) are observed in EEL spectra for
198 nanoparticles separated less than 3 nm due to quantum
199 tunneling effects[41], but this is much lower than the range
200 studied here.
201
202 **Effect of LSPR on Raman signal enhancement**

203   Raman spectra of R6G attached to different particle size
204 arrays were measured with a 532 nm **(Fig. 5b, & S5b)**, a 638
205 nm **(Fig. 5a, & S6)** and a 785 nm laser **(ESI Fig. S6a)** at an
206 optimized power output (**ESI Fig. S10**). The 785 nm laser is
207 medically preferred due to a large tissue penetration
208 depth[42], but clearly shows lower Raman signals for these
209 nanoparticles. The corresponding laser energies are also
210 labelled in **Figs. 3a, & b** as bold vertical lines at the positions
211 of 2.33, 1.94 and 1.58 eV, respectively. To the left of each
212 line, the shaded area represents the range of photon
213 energies collected by the Raman spectrometer. When the
214 excitation laser frequency is close to (and slightly higher
215 than) that of the LSPR of nanoparticles, the Raman signal
216 experiences a significant signal enhancement compared
217 with off-resonance situations. One such example is the 90
218 nm nanodiscs on SiN$_x$ illuminated by a 638 nm laser (**Figs.
219 3a & 5a**), where the energy difference is less than 0.1 eV.
220 The other size arrays under the same illumination show less
221 enhancement as their LSPR energies deviate more from the
222 laser energy. Raman spectra for nanoparticles illuminated
223 by a 785 nm laser are mostly dominated by noise due to
224 inefficient surface plasmon excitation with a laser energy
225 much lower than the LSPR energy (**ESI Fig. S6**). When
226 illuminated by a 532 nm laser, the Raman signal is stronger
227 for smaller diameter arrays, again due to a smaller
228 difference between the laser and LSPR energy (**ESI Fig. S6**).
229 Raman spectra collected from samples on the SiO$_x$
230 membrane illuminated with a 532 nm (**Fig. 5b**) and a 638
231 nm laser (**ESI Fig. S7**) follow the same trend as described for
232 the SiN$_x$ membrane samples. Raman spectra of nanodiscs
233 arrays with different interspacing (**Figs. 4b & S5**) do not
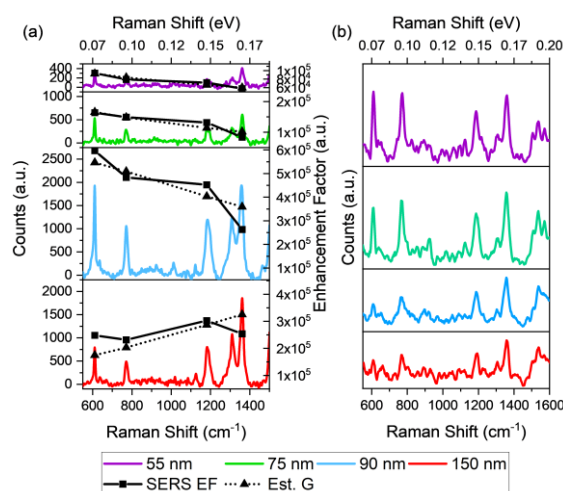
Fig. 5 Raman spectra of R6G attached to nanodisc arrays and comparison with estimated surface plasmon enhancement from EELS. Raman spectra from nanodiscs of different size on **(a)** SiN$_x$ substrates measured with a 638 nm laser and **(b)** SiO$_x$ substrates measured with a 532 nm laser. The highest Raman signal enhancement in (a) occurs for 90 nm diameter nanodiscs. The measured Raman signal enhancement factors (EF, as defined in Methods Equation (2)) at 611 cm^{-1}, 771 cm^{-1}, 1181 cm^{-1} and 1361 cm^{-1} from SERS (square marks) show good agreement with estimated G using Equation (1) above from EELS (triangle marks). For (b), the 75 nm and 55 nm discs enhance Raman signals better than the other arrays. Raman signal EF could not be properly quantified due to the lack of the control Raman spectra because R6G is highly fluorescent at 532 nm laser excitation.

ARTICLE

Table 1. Experimental SERS EF of nanodisc and bowtie arrays tabulated from Fig. 5 and Fig. 7. Reported values of related studies are also included here.

Nanoparticles	Size (nm)	Separation (nm)	SERS EF ($\times 10^5$)	Misc.	References
Au nanodisc arrays	55	75	0.5-0.9	R6G Raman dye, 638 nm laser.	This work.
	75		0.8-1.6		
	90		2.6-6		
	150		2.3-3		
Au periodic nanocylinders	200	25-100	0.25-0.8	pMA Raman dye, 785 nm laser	Gopinath et al.[43]
Inverted Au nanodisc arrays	370	130	4.2	4-MP Raman dye, 785 nm laser	Yu et al.[44]
Au bowtie arrays	70	20	0.6-1.2	R6G Raman dye, 638 nm laser.	This work.
	100		4.0-8.9		
	140		3.3-5.1		
Au bowties	300	30	3.9	Theoretical work, EF derived from electric field enhancement.	Hrtoň et al.[45]
Au bowties arrays	100	6	100	BPE Raman dye, 785 nm laser.	Zhang et al.[46]
		24	1		

234 show much variation in peak enhancement, which agrees
235 with their EELS measurements.
236   Although the observation may be regarded as intuitive,
237 the direct relation between the energy of surface plasmons
238 in EELS and the intensity of Raman signals has not been
239 explicitly shown before to our knowledge. Our observation
240 is also supported by previous work stating that there is no
241 significant spectral shift between the maxima of EELS and
242 optical extinction spectroscopy regarding surface
243 plasmons[47,48]. However, it is reported that the maximum
244 near-field enhancements occur at lower energies than the
245 maximum of the corresponding far-field spectrum due to
246 the system damping in optical studies[22,49]. We suspect
247 similarly lower resonance energy in EELS compared with
248 that in far-field optical measurements, but such a red shift
249 is negligible for the low damping systems investigated here.
250 Furthermore, in biosensing and other practical applications,
251 the maximum Raman signals might be achieved with a
252 lower energy laser than the LSPR energy of nanoparticles
253 due to the competition of extinction effects in solutions
254 against SERS enhancement[50], therefore one of the next
255 steps in our work would be to test the influence of various
256 liquid environments, first by Raman spectroscopy, and then
257 possibly by STEM-EELS using a liquid cell holder. In order to
258 scale up the nanoparticles for real applications, other
259 fabrication methods such as printing, lithography or
260 chemical synthesis, will need to be applied.
261   Another observation is that the Raman peaks are not
262 enhanced uniformly. This is thought to be caused by the
263 variation in local field enhancement at the frequency of
264 different Raman emissions[51]. Following previous studies[3,15],
265 the electromagnetic SERS enhancement G (a ratio of local
266 field intensity at the nanoparticle array to that off the array)
267 is defined by equation:

$$G = I_{Loc}(\omega_L)I_{Loc}(\omega_R) = \frac{|E_{Loc}(\omega_L)|^2}{|E_0(\omega_L)|^2} * \frac{|E_{Loc}(\omega_R)|^2}{|E_0(\omega_R)|^2} \quad (1)$$

268 where I_{Loc} is the local field enhancement at the laser
269 excitation frequency ω_L and the frequency of the Raman
270 peak ω_R. It is safe to approximate $\omega_L = \omega_R$ [15], yielding a
271 fourth-power dependency on local field at laser excitation
272 frequency $G = \left(\frac{E_{Loc}}{E_0}\right)^4$. However, this approximation
273 breaks down at large wavenumbers, especially when the
274 laser energy is in the vicinity of the LSPR energy. The local
275 field enhancement would vary significantly even across a
276 relatively narrow spectrometer collection region. For the
277 150 nm disc array, although the LSPR energy (1.7 eV) is
278 lower than the 638 nm laser energy (1.9 eV), the
279 corresponding Raman modes in the range 1200 cm^{-1} ~1600
280 cm^{-1} (tail of the red shaded area in **Fig. 3a**) are much closer
281 to the LSPR energy, therefore experiencing larger signal
282 enhancement than those in the range 600 cm^{-1} ~800 cm^{-1}.
283 For the 90 nm size array, since the LSPR energy is close to
284 the 638 nm laser energy (**Fig. 3a**), smaller Raman shift peaks
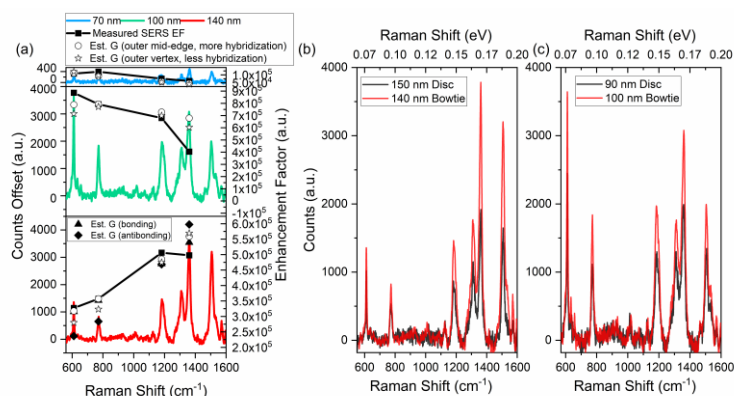285 exhibit stronger enhancement than those for the 150 nm
286 size array.
287   4-MP is also used as a probe molecule to characterize
288 the Raman signal enhancement in addition to R6G and the
289 results are summarized in **ESI Fig. S8, & S9**. The observed
290 trend on the same series of nanodisc arrays follows closely
291 those with R6G, suggesting that the enhancement provided
292 by the nanoparticles is independent on the type of Raman
293 dye.
294   There have been some works relating LSPR from EELS to
295 optical measurements. For example, Husnik et al.[47]
296 reported good agreement between the LSPR of gold
297 antennas measured in EELS and optical extinction
298 spectroscopy. Likewise, Křápek et al.[48] compared EELS of
299 bowties fabricated by focused ion beam with extinction
300 spectra of EBL fabricated bowties and showed good
301 matching of LSPR energy for the transverse dipolar mode.
302 The direct link between light scattering and EELS of surface
303 plasmon excitations in metal spheres was also theoretically
304 demonstrated by modal decomposition[37]. The uniqueness
305 of our work is that we incorporated the linewidth and
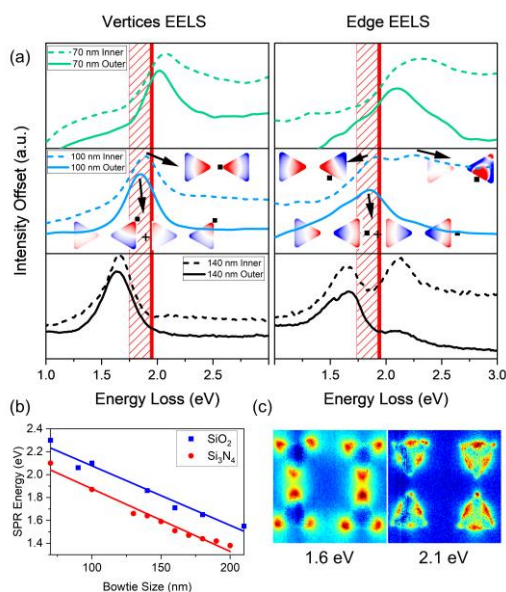
Fig. 6 Experimental EEL spectra of bowtie arrays and LSPR spatial distribution on SiN$_x$. **(a)** EEL spectra at bowtie vertices (left column) and edges (right column) show dipolar (1.5-2 eV) and quadrupolar (2-2.5 eV) modes. The extraction points of EEL spectra are also marked as black squares on the simulated electron density distribution (calculated based on 100 nm bowties with a 50 nm gap), i.e. inner vertices and edge midpoints (dashed lines), as well as outer vertices and edge midpoints (solid lines). Surface plasmon excitation at the inner regions favors antibonding dipolar configuration while the outer regions tend to hybridize the bonding and antibonding dipolar modes (represented by a plus sign of two type electron distributions), resulting in a red-shift of 0.07–0.1 eV for outer dipolar peaks. The gap distance is 20 nm and the triangle height ranges from 70 nm to 140 nm. Simulation details are included in **ESI Fig. 12**. The bold vertical red line and shaded area correspond to the 638 nm (1.94 eV) laser excitation and the Raman spectra collection range from 550–1800 cm^{-1} (0.07–0.22 eV), respectively. **(b)** Dipolar LSPR peak energies vary approximately linearly with bowtie size from 70 to 220 nm measured in EELS and the resonance energy is consistently lower with SiN$_x$ substrates than SiO$_x$ substrates for the same structures. **(c)** EELS intensity map of the 140 nm bowtie at energy loss of 1.6 and 2.1 eV, showing the distribution of the dipolar (left) and the quadrupolar modes (right).

306 intensity of EELS in addition to the plasmon peak positions
307 to correlate and estimate Raman signal enhancement,
308 which leads to a practical way of optimizing nanoparticle
309 parameters for maximum SERS enhancement.

310 A damped harmonic oscillator model was successfully
311 implemented to describe the localized surface plasmon
312 response in both optical spectroscopy[49] and EELS[52], given in
313 the simple form of a Cauchy-Lorentz distribution. The
314 plasmon induced local field enhancement I_{Loc} is essentially
315 the polarizability of the metallic nanostructure[15], which can
316 be derived from the amplitude of the fitted Lorentzian
317 function[49]. In combination with Equation (1), we roughly
318 estimated the SERS enhancement G based on the LSPR
319 energies of different nanodisc sizes, and compared them
320 with experimentally measured enhancement factors (EF) at
321 611 cm^{-1}, 771 cm^{-1}, 1181 cm^{-1} and 1361 cm^{-1} (**Fig. 5a**) using
322 Equation (2). EF and G are comparable in this study because
323 most enhancement comes from the electromagnetic field
324 interaction. The implementation details can be found in the
325 Methods section. Within the same nanodisc array, the
326 estimated G for different Raman emissions follows closely
327 the experimentally measured EF. Our estimation for
328 different nanodisc sizes also reflects their relative Raman
329 peak intensities correctly. Although our model complies
330 with the trend from inter- and intra-array measurements,
331 certain deviations may be caused by (1) uncertainty of
332 Raman peak intensity due to noise and autofluorescence
333 background; (2) far off-resonance excitation as in the case
334 of 150 nm nanodiscs with 532 nm laser excitation.
335 Nonetheless, this simple model provides unique insights
336 into the Raman signal enhancement from EELS data. The
337 experimentally measured EF in **Fig. 5a & 7a** are tabulated
338 along with reported values of related studies[43–45] (**Table 1**).
339 Our optimized nanodiscs show larger EF than the cited
340 highest values in the literature. The EF of our bowties are
341 also at the same level of reported values of similar
342 structures.

343 **Comparison of bowtie arrays and nanodisc arrays**

344 Bowtie arrays, comprised of two sets of equilateral
345 triangles pointing towards each other (**Fig. 1b**), are
346 expected to have stronger Raman enhancement due to the
347 local field confinement and a "lightning rod effect"[15]. They

Fig. 7 Raman spectra and EF of bowtie arrays and comparison with nanodisc arrays. **(a)** R6G Raman spectra of different size bowties and their corresponding SERS EF collected using a 638 nm laser show similar enhancement behavior to that of nanodisc arrays. The estimated G using dipolar peaks from outer vertices is similar to that from outer edge midpoints due to relatively small changes in hybridization. The bonding and antibonding dipolar modes from the outer edge midpoint of 140 nm bowties are deconvolved (ESI. Fig. S13) and the estimated G from the bonding dipolar peak shows better fitting with the measured EF than the antibonding dipolar peak. R6G Raman spectra comparison of **(b)** 150 nm disc and 140 nm bowtie arrays and **(c)** 90 nm disc and 100 nm bowtie arrays illuminated with a 638 nm laser, shows stronger signal enhancement for bowtie arrays under the same collection conditions.

　　　　　　　　　　　　　　　　　　　　　　　　　　　　　ARTICLE

348 were fabricated directly on TEM grids in a similar fashion as
349 for the nanodisc arrays. Most findings from the latter are
350 applicable to bowtie arrays. For example, larger bowtie size
351 and support medium dielectric constant (**Figs. 6a, & b**)
352 result in lower LSPR energy, and the larger interspacing
353 between two pointing vertices has a small effect on red
354 shifting the LSPR energy (**ESI Fig. S11**). However, the
355 reduced symmetry of bowties (compared with discs) allows
356 multiple LSPR modes that can be excited by the electron
357 beam due to the delocalized response and beam
358 broadening effects[53]. **Fig. 6a** shows EEL spectra of different
359 bowtie sizes on SiN_x membranes, extracted from the
360 corresponding black square marked locations of the
361 simulated charge density map. The dipolar peaks from
362 outer regions (away from the gap, solid lines) are
363 approximately 0.07–0.1 eV lower than those from inner gap
364 regions (dashed lines) because of hybridization of bonding
365 and anti-bonding dipole configurations[54]. At inner-gap
366 vertices only the anti-bonding dipolar mode is excited as
367 indicated by the electron density distributions[27,55]. The peak
368 positions of bonding and antibonding dipolar modes of 140
369 nm bowties are spectrally visible at 1.54 and 1.64 eV
370 respectively (**Fig. 6a**) and subsequently fitted using two
371 Voigt functions (**ESI Fig. S13**). An additional transverse
372 dipolar mode at even lower energy is reported for focused-
373 ion beam fabricated bowties comprised of right triangles
374 when excited at outer vertices[48], but not observed here due
375 to the symmetry of equilateral triangles. Interestingly,
376 nanodiscs and bowties of similar size also have roughly
377 similar LSPR energies (**Fig. 3a, & 6a**). Additional results on
378 dipolar LSPR energies as a function of bowtie size from 70
379 nm to 220 nm are plotted in **Fig. 6b** for structures on SiN_x
380 and SiO_x substrates. Just like nanodisc arrays, the LSPR
381 energy of the same structures is higher on the SiO_x than on
382 the SiN_x substrates due to the difference in dielectric
383 constants.

384　　　An additional mode at energy loss 2.0–2.5 eV in **Fig. 6a**
385 when excited at the midpoints of inner edges can be
386 attributed to a quadrupolar configuration[27]. **Fig. 6c** shows
387 the spatial distribution of the dipolar LSPR mode (at 1.6 eV)
388 and dark quadrupolar LSPR mode (at 2.1 eV) in a 140 nm
389 bowtie extracted from an EELS spectrum image. These
390 results show that the strongest dipolar modes reside on
391 triangle vertices while the quadrupolar modes primarily
392 reside along the sides of the bowties. More detailed
393 discussion of different plasmon modes in triangular arrays
394 can be found in the previous study by Koh et al.[27]

395　　　The Raman enhancement behavior from dipolar surface
396 plasmons is similar for both bowties and nanodiscs, as
397 illustrated by the Raman spectra (**Fig. 7a**) collected using a
398 638 nm laser for different size bowties on a SiN_x substrate.
399 100 nm bowtie arrays have overall strongest signal
400 enhancement due to close match between the incident
401 laser energy and dipolar LSPR energy. The quadrupolar
402 mode is believed to be a dark mode[26,27] and thus should
403 have insignificant effect on Raman signal enhancement (**ESI**
404 **Fig. S14**). The measured EF of four Raman emissions are also

405 plotted in **Fig. 7a**. Using the same damped harmonic
406 oscillator model, the calculated enhancement G based on
407 the less hybridized dipolar surface plasmon peaks on outer
408 vertices deviates away from the EF at small wavenumbers
409 (611 cm^{-1}), while it agrees better at large wavenumbers
410 (1361 cm^{-1}) compared with that based on the more
411 hybridized plasmons on the corresponding outer edge
412 midpoints for the 100 nm bowties. Overall, G from outer
413 vertices does not differ much from outer edge midpoints
414 due to relatively small changes in hybridization. However, a
415 preliminary estimation of G from the bonding dipolar mode
416 shows better agreement with experimentally measured EF
417 than that from the antibonding dipolar mode for 140 nm
418 sized bowtie arrays (**Fig. 7a**) based on the fitted peaks in **ESI**
419 **Fig. S13** (details in Methods), suggesting that the bonding
420 dipolar mode is the dominant factor for enhancement
421 under the laser excitation. This is reasonable because the
422 antibonding mode is a dark mode and therefore would not
423 be efficiently excited with a laser. Besides, the electric field
424 in the gap is only strongly enhanced by the bonding dipole
425 mode, but not the antibonding mode[56]. Hence, the
426 measured EF would mainly reflect bonding mode behavior.
427 Future studies can aim to further test the relation of SERS
428 EF and estimated G from antibonding dipolar, transverse
429 and longitudinal dipolar, and other surface plasmon modes
430 using higher energy resolution STEM-EELS and polarized
431 Raman spectroscopy on less symmetric nanostructures.

432　　　A rough comparison of Raman spectra between
433 approximately similar sized nanodisc and bowtie arrays
434 under the same illumination conditions (**Fig. 7b, c**) shows
435 higher signal enhancement for bowtie arrays due to the
436 stronger electric field near the sharp vertices, given that
437 their LSPR energy difference is small. Similar behavior is also
438 observed in other geometric configurations such as
439 plasmonic heterodimers for SERS hotspots[57], where the
440 separation gap is extremely small (< 5 nm). However, the
441 shape effect on Raman signal enhancement is weaker for
442 small size arrays (**Fig. 6c**) than that for large size arrays (**Fig.
443 6b**), possibly due to the decline of fabrication quality as
444 nanostructure features become smaller.

Conclusions

446　　　In summary, we have systematically varied gold
447 nanoparticle size, interspacing and shape using electron
448 beam lithography fabrication, and showed that these
449 nanoparticle parameters as well as local dielectric
450 environment affect surface plasmon resonance.
451 Nanoparticle size plays the most important role in fine-
452 tuning the resonance energy. Pointed structure shapes
453 have stronger field confinement and therefore strongly
454 enhance the Raman signal. By correlating LSPR energies
455 from EELS with Raman peaks from laser excitation, we
456 demonstrate that the Raman signal is most strongly
457 enhanced when the illuminating laser energy is close to and
458 slightly higher than the LSPR energy, as in the case of 90 nm
459 nanodisc arrays measured with a 638 nm laser. Using

460 monochromated STEM-EELS, this study brings insight from
461 nanometer level spatial distribution of localized surface
462 plasmons to far-field surface enhanced Raman
463 spectroscopy. We anticipate that the techniques and
464 correlations demonstrated in this study will provide a set of
465 tools and guidelines to optimize Raman signal enhancement
466 in real applications such as nanomedicine for cancer
467 diagnostics and treatment[11,13].

Methods

469 Nanostructure array fabrication

470   TEM grids with SiN_x and SiO_x membranes (Ted Pella Inc.,
471 35 nm thick) were first plasma cleaned to remove potential
472 organic contaminants. They were then adhered to a piece
473 of silicon wafer using polydimethylsiloxane and spin coated
474 with 2% 950 kDa PMMA (E-beam resist) in anisole at 2500
475 rpm followed by baking for 5 min at 180 °C. The samples
476 were loaded near the center of a slot holder and a JEOL JBX
477 6300 E-beam lithography system (JEOL, Ltd, Japan) was
478 operated as a scanning electron microscope (SEM) to locate
479 the small electron transparent windows. To limit random
480 electron exposure on the patterning area, the stage
481 positions of two opposite corners of the grid were carefully
482 found to roughly calculate the coordinates of the grid
483 center. The lithography system was then switched to
484 pattern writing mode with a 100 kV 500 pA beam and an
485 average dose of 2000 $\mu C/cm^2$. The overall pattern
486 resolution is approximately 9 nm. The patterns of nanodisc
487 and bowtie arrays with different size and spacing were
488 described in a proprietary format from JEOL and rendered
489 into exposable files using BEAMER software (GenISys
490 GmbH, Germany). After lithography, the samples were
491 submerged in a 1:3 methyl isobutyl ketone/2-propanol
492 solution for 30 s to selectively dissolve the patterned region
493 while keeping the remaining PMMA intact as a mask for
494 metallization. The samples were then rinsed in 2-propanol
495 and blown dry with compressed air. To avoid the damping
496 effect of a metallic adhesion layer, an organic alternative,
497 (3-mercaptopropyl) trimethoxysilane (MPTMS) was applied
498 by vapor deposition [32]. Gold depositions were performed in
499 a Kurt J Lesker E-beam evaporator, and film thickness of
500 roughly 30 nm was reported by a crystal monitor. A lift-off
501 process was carried out in an acetone bath to strip away the
502 PMMA mask and leave only the Au in the patterned
503 (unmasked) region. Samples were rinsed in deionized water
504 and dried with compressed air.

505 Electron energy loss spectroscopy

506   STEM-EELS spectrum images were collected in an image
507 C_s corrected monochromated FEI Titan (Thermo Fisher
508 Scientific, USA) at 300 kV with a Gatan Image Filter (GIF)
509 Quantum (Gatan, Inc, USA) EEL spectrometer. The
510 microscope was operated in STEM mode at a spot size of 11
511 with a C2 aperture of 150 μm and a C3 aperture of 50 μm,
512 resulting in a convergence semi-angle of 8.4 mrad and an

513 estimated beam size of 0.5 nm in diameter. The GIF
514 Quantum was operated in EELS mode with a 2.5 mm
515 entrance aperture and a camera length of 38 mm
516 (corresponding to a collection angle of 18.3 mrad). EELS
517 maps were collected with a 2 nm pixel size and 0.01
518 eV/channel dispersion over a typical 100 × 100 array. The
519 full width at half maximum (FWHM) of the zero loss peak
520 (ZLP) was measured to be from 0.13 to 0.2 eV throughout
521 the experiments. Spectral collection time was selected to
522 maximize the signal without saturating the EELS detector,
523 which is about 2 ms dwell time for this system.

524 Surface enhanced Raman spectroscopy

525   All samples were submerged in a 0.1 mg/mL aqueous
526 solution of Rhodamine 6G (R6G) or 4-mercaptopyridine (4-
527 MP) overnight, rinsed in deionized water and blown dry
528 with compressed air. Raman spectroscopy was performed
529 on a Horiba XploRA+ system using a 100X objective lens to
530 focus the laser beam to the smallest possible spot (~2 μm),
531 which is roughly the same as the nanostructure array size.
532 An output power of 0.6 mW for the 532 nm laser, 1.7 mW
533 for the 638 nm laser, and 8 mW for the 785 nm laser were
534 carefully chosen to avoid ablation (described in SI **Fig. 7**)
535 while still maintaining reasonable signal to noise ratio.
536 Spectral acquisition time was optimized accordingly, and
537 each spectrum was accumulated three times to reduce
538 noise and artifacts. Raman spectra were not normalized,
539 but the comparison was based on the same acquisition
540 conditions. The enhancement factor (EF, a ratio of surface
541 enhanced Raman intensity to the control sample Raman
542 intensity) for rhodamine 6G (R6G) was calculated using the
543 following formula:

$$EF = \left(\frac{I_{SERS}}{I_{bulk}}\right) * \left(\frac{N_{bulk}}{N_{surf}}\right) \qquad (2)$$

544 Where I_{SERS} and I_{bulk} are the measured peak intensities in
545 the SERS and control Raman spectra of R6G respectively.
546 N_{bulk} and N_{surf} are the number of molecules under laser
547 illumination for the bulk and SERS sample, respectively. In
548 our setup, the bulk sample is 10 mg/mL R6G water solution
549 in a cuvette with 1 mm optical path (Raman spectrum in **ESI**
550 **Fig. S4**). The laser spot is estimated as a 2 μm diameter
551 circle, therefore N_{bulk} is roughly 4×10^{10} molecules. It is
552 reported that the average surface density of R6G in densely
553 packed monolayers is approximately $4 \times 10^{-11} \ mol/cm^2$
554 [58], thus we estimated N_{surf} on the 2 $\mu m \times 2 \ \mu m$ array to
555 be 10^6. Although recent work demonstrated STEM-EELS
556 could be used to map the adsorbed surface molecules[59], it
557 is difficult to achieve for Raman dyes because these organic
558 molecules are known to aggregate and build up as carbon
559 contamination when exposed to an electron beam.
560   The fluorescence background of measured Raman
561 spectra were fitted as polynomial functions and
562 subsequently removed using a MATLAB script[60], before
563 extracting the peak intensities to compute the

564 enhancement factors. The script is available online at
565 https://github.com/michaelstchen/modPolyFit.

Hyperspectral data processing

567 EEL spectrum images were analyzed in Gatan
568 Microscopy Suite (GMS) 3 (Gatan Inc.). The reflected tail
569 method implemented in the software was used for zero loss
570 peak (ZLP) subtraction. EEL spectra were normalized with
571 respect to the ZLP maximum intensity. EELS intensities at a
572 particular energy loss were plotted in a colormap using a
573 MATLAB script. Spectrum images were imported into
574 MATLAB using a modified version of the algorithm available
575 online at
576 https://www.mathworks.com/matlabcentral/fileexchange
577 /29351.

EELS simulation

579 EELS simulations were calculated using the MNPBEM
580 toolbox[34] with the retarded approximation, similar to a
581 previously reported approach[20]. These calculations utilized
582 electron beam parameters consistent with the experiment,
583 including an energy of 300 keV and a probe diameter of 0.5
584 nm. EEL spectra were calculated using an electron beam
585 positioned at similar locations as those used in the
586 experiment and with an energy step of 0.01 eV. The Au
587 nanodisc arrays were modelled as a nine disc array
588 positioned on top of a substrate layer. The number of discs
589 in the array was limited to nine because of computational
590 limitation. However, it was found that a nine-disc array was
591 sufficient for the simulation to closely match the
592 experimental observation. Additionally, increasing the
593 array size from four to nine discs had very minor effects on
594 the simulated results, suggesting that nine discs are
595 sufficient for capturing the behaviour of EELS signals from
596 these samples. The geometry of the Au disc array models,
597 for example the disc diameter and disc spacing, were
598 created to be consistent with STEM observations. The single
599 discs were generated from a 20-sided polygon positioned
600 on top of a 35 nm thick layer of SiN_X or SiO_X. Energy-
601 dependent dielectric values adapted from literature were
602 used for Au[61]. A dielectric constant of 4.2 and 2.1 were used
603 for the SiN_X and SiO_X substrates, respectively. The bowtie
604 models were created from two triangular shaped plates
605 that had a thickness of 30 nm, a length of 100 nm, and a
606 corner radius of 10 nm, similar to the experimentally
607 observed structures. The bowtie was given a 50 nm gap and
608 placed on a 35 nm thick SiN_X substrate. The surrounding
609 medium for all models used a vacuum dielectric constant of
610 1.
611 To simulate the spectral broadening caused by the
612 experimental EELS energy resolution, simulated spectra
613 were convolved with a Lorentzian function at a full width
614 half maxima between 0.13 and 0.2 eV that was measured
615 from the corresponding experimental data. Simulated EELS
616 maps, such as those shown in **Figs. 2d-e**, were calculated in
617 the area around the central disc of a 9 disc array. Then the
618 simulated map was reproduced 4 times to make it more

619 comparable to the experimentally mapped areas. To help
620 interpret the experimentally measured LSPR modes, the
621 complex charge distribution for each mode was studied.
622 Both the real and imaginary parts of the complex charge
623 distributions were calculated for each mode, but only the
624 imaginary part of the charge distribution is presented here,
625 following previous studies[20,62].

Damped harmonic oscillator model

627 Electron energy loss ΔE can be computed from the work
628 performed by the electron against the induced electric
629 field E_{ind}[63]
630 $\Delta E = e \int v \cdot E_{ind}[r(t), t]dt = \int \hbar \omega \Gamma_{EELS}(R, \omega)d\omega$,
631 where v is the speed of electrons, $r(t)$ denotes the time
632 dependent position function and the loss probability
633 $\Gamma_{EELS}(R, \omega) = \int \mathcal{R}e\{e^{-i\omega t} v \cdot E_{ind}[r(t), \omega]\}dt$ is the work
634 done by electrons in Fourier space with ω being their
635 frequency. That is, the amplitude of EEL spectra is related
636 to the local induced electric field. Moreover, it has recently
637 been shown that in systems with translational invariance
638 along the direction of electron motion, the electron energy
639 loss probability is proportional to the photonic local density
640 of states[64], the property of which again has been proven to
641 be proportional to the local field intensity normalized by the
642 absorbed power[65]. Considering that a damped harmonic
643 oscillator can be used to model the local field enhancement
644 in optical studies[49], we therefore use a similar approach to
645 describe the LSPR response in EELS given by

$$I(\omega) = \frac{A}{(\omega - \omega_p)^2 + \left(\frac{\Gamma}{2}\right)^2} \qquad (3)$$

646 where $I(\omega)$ is the frequency dependent polarizability of the
647 oscillator, which we also take as the local field
648 enhancement in this context[15,49]. A is a proportionality
649 factor, ω_p is the plasmon frequency, and Γ is the FWHM of
650 the resonance, which is a measure of the total damping of
651 the system. One of the challenges when applied in EELS is
652 the instrument broadening effects on the resonance
653 linewidth Γ due to the non-monochromaticity of the
654 electron source. Here we used Olivero and Longbothum's
655 empirical approach[52,66] by assuming the ZLP is a Gaussian
656 function and the LSPR follows a Lorentzian profile.

$$\Gamma_V = 0.53\Gamma_L + \sqrt{0.22\Gamma_L^2 + \Gamma_G^2} \qquad (4)$$

657 where Γ_V is the FWHM of the convolved surface plasmon
658 peak which produces a Voigt profile, Γ_G is the FWHM of the
659 ZLP and Γ_L is approximately the original surface plasmon
660 linewidth. The convolved plasmon peak was fitted into a
661 Voigt profile using OriginPro software to obtain Γ_V values.
662 (For bowties, both the bonding and antibonding dipolar
663 surface plasmon peaks were fitted and each peak was
664 analyzed separately using the same method as the
665 following). The calculated LSPR linewidth along with the
666 resonance energy were then inserted into Equation (3) to
667 estimate the local field enhancement. Although the surface

668 plasmons driven by electrons are different from those by
669 plane waves, the differences are more related to the spatial
670 distribution of hotspots[67,68]. In our study as well as other
671 published work that correlate optical and EEL
672 spectroscopy[69,70] where traditional hotspots are not
673 considered, the localized surface plasmon resonance for
674 disperse nanoparticles are reasonably similar in both types
675 of excitation. Therefore using Equation (1), the
676 electromagnetic SERS enhancement G can be roughly
677 estimated from EEL spectra as $I(\omega_L)I(\omega_R)$, where ω_L is the
678 laser excitation frequency and ω_R is the Raman peak
679 frequency. To directly compare the measured SERS EF and
680 the estimated G from EELS in **Fig. 5a**, a scaling constant k is
681 applied to our estimated G by minimizing the sum of the
682 squares of the difference between measured EF and
683 estimated G.

Conflicts of interest

685 There are no conflicts to declare.

Acknowledgements

## Notes and references

703 1   M. Fleischmann, P. J. Hendra and A. J. McQuillan,
704   *Chem. Phys. Lett.*, 1974, **26**, 163–166.
705 2   S. Nie and S. R. Emory, *Science*, 1997, **275**, 1102–1106.
706 3   K. Kneipp, H. Kneipp, I. Itzkan, R. D. Ramachandra and
707   S. F. Michael, *J. Phys. Condens. Matter*, 2002, **597**,
708   597–624.
709 4   K. Kneipp, Y. Wang, H. Kneipp, L. T. Perelman, I. Itzkan,
710   R. R. Dasari and M. S. Feld, *Phys. Rev. Lett.*, 1997, **78**,
711   1667.
712 5   R. M. Jarvis, A. Brooker and R. Goodacre, *Faraday
713   Discuss.*, 2006, **132**, 281–292.
714 6   B. Sharma, R. R. Frontiera, A.-I. Henry, E. Ringe and R.
715   P. Van Duyne, *Mater. today*, 2012, **15**, 16–25.
716 7   Z. A. Nima, M. Mahmood, Y. Xu, T. Mustafa, F.
717   Watanabe, D. A. Nedosekin, M. A. Juratli, T. Fahmi, E. I.
718   Galanzha, J. P. Nolan, A. G. Basnakian, V. P. Zharov and
719   A. S. Biris, *Sci. Rep.*, 2014, **4**, 4752(1–8).
720 8   Z. Wang, S. Zong, L. Wu, D. Zhu and Y. Cui, *Chem. Rev.*,
721   2017, **117**, 7910–7963.
722 9   J. V Jokerst, A. J. Cole, D. Van de Sompel and S. S.
723   Gambhir, *ACS Nano*, 2012, **6**, 10366–10377.
724 10   C. L. Zavaleta, B. R. Smith, I. Walton, W. Doering, G.
725   Davis, B. Shojaei, M. J. Natan and S. S. Gambhir, *Proc.
726   Natl. Acad. Sci.*, 2009, **106**, 13511–13516.
727 11   M. F. Kircher, A. De La Zerda, J. V. Jokerst, C. L.
728   Zavaleta, P. J. Kempen, E. Mittra, K. Pitter, R. Huang, C.
729   Campos, F. Habte, R. Sinclair, C. W. Brennan, I. K.
730   Mellinghoff, E. C. Holland and S. S. Gambhir, *Nat.
731   Med.*, 2012, **18**, 829–834.
732 12   J. V Jokerst, A. J. Cole, S. E. Bohndiek and S. S.
733   Gambhir, in *Photons Plus Ultrasound: Imaging and
734   Sensing 2014*, International Society for Optics and
735   Photonics, 2014, vol. 8943, p. 894366.
736 13   H. Arami, C. B. Patel, S. J. Madsen, P. J. Dickinson, R. M.
737   Davis, Y. Zeng, B. K. Sturges, K. D. Woolard, F. G.
738   Habte, D. Akin, R. Sinclair and S. S. Gambhir, *ACS Nano*,
739   2019, **13**, 2858–2869.
740 14   A. S. Thakor, R. Luong, R. Paulmurugan, F. I. Lin, P.
741   Kempen, C. Zavaleta, P. Chu, T. F. Massoud, R. Sinclair
742   and S. S. Gambhir, *Sci. Transl. Med.*, 2011, **3**, 79ra33-
743   79ra33.
744 15   S. A. Maier, in *Plasmonics: Fundamentals and
745   Applications*, Springer US, New York, NY, 2007, pp. 65–
746   88.
747 16   S. A. Maier, M. L. Brongersma, P. G. Kik and H. A.
748   Atwater, *Phys. Rev. B*, 2002, **65**, 193408.
749 17   G. A. Wurtz, J. S. Im, S. K. Gray and G. P. Wiederrecht,
750   *J. Phys. Chem. B*, 2003, **107**, 14191–14198.
751 18   S. C, F. T, W. T, von P. G, F. J, C. Sönnichsen, T. Franzl,
752   T. Wilk, G. Von Plessen and J. Feldmann, *New J. Phys.*,
753   2002, **4**, 93.
754 19   J. J. Mock, M. Barbic, D. R. Smith, D. A. Schultz and S.
755   Schultz, *J. Chem. Phys.*, 2002, **116**, 6755–6759.
756 20   A. B. Yankovich, R. Verre, E. Olsén, A. E. O. Persson, V.
757   Trinh, G. Dovner, M. Käll and E. Olsson, *ACS Nano*,
758   2017, **11**, 4265–4274.
759 21   R. A. Alvarez-Puebla, *J. Phys. Chem. Lett.*, 2012, **3**, 857–
760   866.
761 22   A. D. McFarland, M. A. Young, J. A. Dieringer and R. P.
762   Van Duyne, *J. Phys. Chem. B*, 2005, **109**, 11279–11285.
763 23   P. L. Stiles, J. A. Dieringer, N. C. Shah and R. P. Van
764   Duyne, *Annu. Rev. Anal. Chem.*, 2008, **1**, 601–626.
765 24   H. Kuwata, H. Tamaru, K. Esumi and K. Miyano, *Appl.
766   Phys. Lett.*, 2003, **83**, 4625–4627.
767 25   H. Ditlbacher, A. Hohenau, D. Wagner, U. Kreibig, M.
768   Rogers, F. Hofer, F. R. Aussenegg and J. R. Krenn, *Phys.
769   Rev. Lett.*, 2005, **95**, 257403.
770 26   J. Nelayah, M. Kociak, O. Stéphan, F. J. G. De Abajo, M.
771   Tencé, L. Henrard, D. Taverna, I. Pastoriza-Santos, L.
772   M. Liz-Marzán, C. Colliex, A. D. E. Abajo, F. J. G. I, C.
773   Colliex, L. M. L. An, L. De Physique and C. Umr, *Nat.
774   Phys.*, 2007, **3**, 348.

775 27   A. L. Koh, A. I. Fernández-Domínguez, D. W. Mccomb,
776   S. A. Maier, J. K. W. Yang, A. I. Fern, D. W. Mccomb, S.
777   A. Maier and J. K. W. Yang, *Nano Lett.*, 2011, **11**, 1323–
778   1330.
779 28   M. Bosman, V. J. Keast, M. Watanabe, A. I. Maaroof
780   and M. B. Cortie, *Nanotechnology*, 2007, **18**, 165505.
781 29   J. A. Scholl, A. L. Koh and J. A. Dionne, *Nature*, 2012,
782   **483**, 421.
783 30   E. P. Bellido, A. Manjavacas, Y. Zhang, Y. Cao, P.
784   Nordlander and G. A. Botton, *ACS Photonics*, 2016, **3**,
785   428–433.
786 31   T. Putnin, C. Lertvachirapaiboon, R. Ishikawa, K.
787   Shinbo, K. Kato, S. Ekgasit, K. Ounnunkad and A. Baba,
788   *Opto-Electronic Adv.*, 2019, **2**, 190010.
789 32   S. J. Madsen, M. Esfandyarpour, M. L. Brongersma and
790   R. Sinclair, *ACS Photonics*, 2017, **4**, 268–274.
791 33   D. Serien and K. Sugioka, *Opto-Electronic Reports*,
792   2018, **4**, a201804002.
793 34   U. Hohenester and A. Trügler, *Comput. Phys.
794   Commun.*, 2012, **183**, 370–381.
795 35   F.-P. Schmidt, H. Ditlbacher, U. Hohenester, A.
796   Hohenau, F. Hofer and J. R. Krenn, *Nano Lett.*, 2012,
797   **12**, 5780–5783.
798 36   K. L. Kelly, E. Coronado, L. L. Zhao and G. C. Schatz, *J.
799   Phys. Chem. B*, 2003, **107**, 668–677.
800 37   S. M. Collins and P. A. Midgley, *Phys. Rev. B - Condens.
801   Matter Mater. Phys.*, 2013, **87**, 235432.
802 38   G. D. Bernasconi, J. Butet, V. Flauraud, D. Alexander, J.
803   Brugger and O. J. F. Martin, *ACS Photonics*, 2017, **4**,
804   156–164.
805 39   K. Luke, Y. Okawachi, M. R. E. Lamont, A. L. Gaeta and
806   M. Lipson, *Opt. Lett.*, 2015, **40**, 4823–4826.
807 40   I. H. Malitson, *Josa*, 1965, **55**, 1205–1209.
808 41   J. A. Scholl, A. García-Etxarri, A. L. Koh and J. A. Dionne,
809   *Nano Lett.*, 2013, **13**, 564–569.
810 42   A. M. Smith, M. C. Mancini and S. Nie, *Nat.
811   Nanotechnol.*, 2009, **4**, 710–711.
812 43   A. Gopinath, S. V Boriskina, B. M. Reinhard and L. Dal
813   Negro, *Opt. Express*, 2009, **17**, 3741–3753.
814 44   Q. Yu, P. Guan, D. Qin, G. Golden and P. M. Wallace,
815   *Nano Lett.*, 2008, **8**, 1923–1928.
816 45   M. Hrtoň, A. Konečná, M. Horák, T. Šikola and V.
817   Křápek, *Phys. Rev. Appl.*, 2020, **13**, 054045.
818 46   J. Zhang, M. Irannejad and B. Cui, *Plasmonics*, 2015,
819   **10**, 831–837.
820 47   M. Husnik, F. Von Cube, S. Irsen, S. Linden, J.
821   Niegemann, K. Busch and M. Wegener,
822   *Nanophotonics*, 2013, **2**, 241–245.
823 48   V. Křápek, A. Konečná, M. Horák, F. Ligmajer, M.
824   Stöger-Pollach, M. Hrtoň, J. Babocký and T. Šikola,
825   *Nanophotonics*, 2019, **9**, 623–632.
826 49   J. Zuloaga and P. Nordlander, *Nano Lett.*, 2011, **11**,
827   1280–1283.
828 50   S. T. Sivapalan, B. M. DeVetter, T. K. Yang, T. Van Dijk,
829   M. V Schulmerich, P. S. Carney, R. Bhargava and C. J.
830   Murphy, *ACS Nano*, 2013, **7**, 2099–2105.
831 51   D. Cialla, J. Petschulat, U. Hübner, H. Schneidewind, M.
832   Zeisberger, R. Mattheis, T. Pertsch, M. Schmitt, R.
833   Möller and J. Popp, *ChemPhysChem*, 2010, **11**, 1918–
834   1924.
835 52   M. Bosman, E. Ye, S. F. Tan, C. A. Nijhuis, J. K. W. W.
836   Yang, R. Marty, A. Mlayah, A. Arbouet, C. Girard and
837   M.-Y. Y. Han, *Sci. Rep.*, 2013, **3**, 1312.
838 53   A. Hörl, A. Trügler and U. Hohenester, *ACS photonics*,
839   2015, **2**, 1429–1435.
840 54   I. Alber, W. Sigle, S. Müller, R. Neumann, O. Picht, M.
841   Rauber, P. A. Van Aken and M. E. Toimil-Molares, *ACS
842   Nano*, 2011, **5**, 9845–9853.
843 55   N. Mirsaleh-Kohan, V. Iberi, P. D. Simmons, N. W.
844   Bigelow, A. Vaschillo, M. M. Rowland, M. D. Best, S. J.
845   Pennycook, D. J. Masiello, B. S. Guiton and J. P.
846   Camden, *J. Phys. Chem. Lett.*, 2012, **3**, 2303–2309.
847 56   W. Yang, Y. F. Chou Chau and S. C. Jheng, *Phys.
848   Plasmas*, 2013, **20**, 064503.
849 57   Y. Tian, Z. Shuai, J. Shen, L. Zhang, S. Chen, C. Song, B.
850   Zhao, Q. Fan and L. Wang, *Small*, 2018, **14**, 1800669.
851 58   A. Kudelski, *Chem. Phys. Lett.*, 2005, **414**, 271–275.
852 59   W.-C. D. Yang, C. Wang, L. A. Fredin, P. A. Lin, L.
853   Shimomoto, H. J. Lezec and R. Sharma, *Nat. Mater.*,
854   2019, **18**, 614–619.
855 60   J. Zhao, H. Lui, D. I. McLean and H. Zeng, *Appl.
856   Spectrosc.*, 2007, **61**, 1225–1232.
857 61   P. B. Johnson and R.-W. Christy, *Phys. Rev. B*, 1972, **6**,
858   4370.
859 62   D. Knebl, A. Hörl, A. Trügler, J. Kern, J. R. Krenn, P.
860   Puschnig and U. Hohenester, *Phys. Rev. B*, 2016, **93**,
861   81405.
862 63   R. H. Ritchie, *Phys. Rev.*, 1957, **106**, 874.
863 64   F. J. García De Abajo, M. Kociak, F. J. G. De Abajo and
864   M. Kociak, *Phys. Rev. Lett.*, 2008, **100**, 1–4.
865 65   T. V. Shahbazyan, *Phys. Rev. Lett.*, 2016, **117**, 207401.
866 66   J. J. Olivero and R. L. Longbothum, *J. Quant. Spectrosc.
867   Radiat. Transf.*, 1977, **17**, 233–236.
868 67   N. W. Bigelow, A. Vaschillo, V. Iberi, J. P. Camden and
869   D. J. Masiello, *ACS Nano*, 2012, **6**, 7497–7504.
870 68   U. Hohenester, H. Ditlbacher and J. R. Krenn, *Phys.
871   Rev. Lett.*, 2009, **103**, 106801.
872 69   V. Myroshnychenko, J. Nelayah, G. Adamo, N.
873   Geuquet, J. Rodríguez-Fernández, I. Pastoriza-Santos,
874   K. F. MacDonald, L. Henrard, L. M. Liz-Marzán and N. I.
875   Zheludev, *Nano Lett.*, 2012, **12**, 4172–4180.
876 70   B. S. Guiton, V. Iberi, S. Li, D. N. Leonard, C. M. Parish,
877   P. G. Kotula, M. Varela, G. C. Schatz, S. J. Pennycook
878   and J. P. Camden, *Nano Lett.*, 2011, **11**, 3482–3488.
879
880
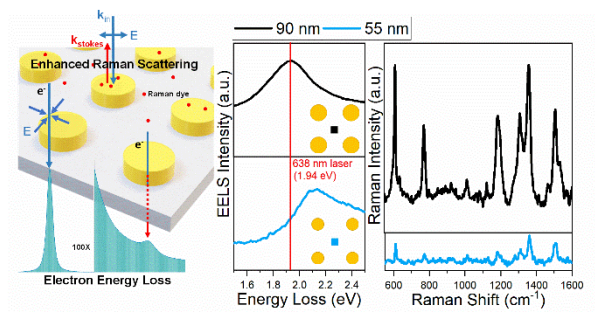
Correlation of surface plasmon resonance and surface enhanced Raman scattering: maximum enhancement achieved when excitation laser match with plasmon resonance.